

FEATURE ARTICLE

Femtosecond Studies of Electron Dynamics at Dielectric-Metal Interfaces

C. M. Wong, J. D. McNeill, K. J. Gaffney, N.-H. Ge, A. D. Miller, S. H. Liu, and C. B. Harris*

*Department of Chemistry, University of California, Berkeley, California 94720, and Chemical Sciences Division, E. O. Lawrence Berkeley National Laboratory, Berkeley, California 94720**Received: September 30, 1998*

Ultrafast relaxation dynamics of electrons at dielectric-metal interfaces reflect the nature of the electronic interaction with both the substrate and the adsorbed layer. The full understanding of macroscopic electrical transport properties across an interface requires the knowledge of the energies, spatial extent of the interfacial electronic states, and the electron scattering length. With the femtosecond two-photon photoemission technique, it is possible to directly observe the dynamics of interfacial electrons with specific energy and parallel momentum. Interband and intraband electron relaxation dynamics in excited surface and quantum well states are determined with momentum and time-resolved two-photon photoemission. The study of charge carrier scattering at interfaces and in ultrathin films of Xe on Ag(111) provides a wealth of information on the energy, parallel momentum, and layer thickness dependence of the electron scattering rate. Adsorption of Xe on metal surfaces modifies the interfacial potential and drastically changes the spatial extent of the interfacial electronic wavefunction. The spatial extent of the electronic wavefunction in the direction perpendicular to the interface determines the interband relaxation rate. Oscillation in the interband relaxation time as a function of layer thickness is attributed to a quantum size effect. The lifetime of the $n = 1$ surface state shows a strong parallel momentum dependence. This phenomenon is attributed to intraband momentum relaxation. The thickness dependence of intraband relaxation suggests a change in the scattering potential in the direction parallel to the interface for a monolayer and bilayer of Xe. The possibility of scattering due to thermal and structural disorder is discussed.

1. Introduction

Electrons at interfaces provide a unique opportunity to study the importance of reduced dimensionality and electron confinement on carrier dynamics. Fundamental and technological understanding of the transport properties of electrons across device junctions requires knowledge of electron scattering, relaxation, and recombination processes at surfaces and interfaces. In addition, electron interactions with interfaces govern fundamental aspects of surface chemical and electrochemical processes. For example, the breaking of chemical bonds at surfaces can be induced by electron transfer from the substrate to dissociative states of the surface molecules, which causes fragmentation and/or desorption of adsorbates.¹ There are other areas of study in which the interaction of charges with metal–insulator interfaces are important, such as the screening effects of an insulator in ion desorption and the determination of electronic structure of metal–organic device junctions. Xe on a metal surface is a model system for the study of the effects of thin insulating films on a conductor. The attractive electron affinity of bulk Xe results in quantum well states that confine electrons to the plane parallel to the interface. Thus the study of Xe quantum well electron dynamics provides a means for investigating the effect of quantum confinement on electron transport in a layer-by-layer fashion.

Most of the tools in surface science, such as scanning tunneling microscopy, scanning force microscopy, electron

energy loss, and Auger emission involve the interaction of electrons at surfaces. These techniques, however, lack the time resolution necessary to directly measure electron dynamics across surfaces and interfaces. Recently, the development of femtosecond two-photon photoemission (TPPE) spectroscopy and its application to a variety of systems have immensely increased our knowledge of surface electron dynamics. Studies of surface state electrons at metal–dielectric,² metal–semiconductor,³ and metal–metal⁴ interfaces using TPPE have been reviewed. In TPPE spectroscopy, electrons are excited from occupied states of the substrate by an excitation pulse into unoccupied surface states and photoemitted from these surface states by a probe pulse. The photoemission intensity of the unoccupied surface state as a function of time delay between the pump pulse and the probe pulse directly reveals the electron dynamics of the surface state. This technique combined with angle resolution allows the mapping of the band structure of unoccupied energy bands at interfaces and the study of electron dynamics as a function of electron parallel momentum. Electrons with non-zero parallel momentum exhibit decay pathways that arise from scattering of the electrons with surface defects and phonons at the interface. The scattering rate strongly depends on the electron velocity or momentum in the surface parallel.

Image state electrons (see section 1.1) can be used as probes of the electronic structure and dynamics at surfaces. Image states are extended states or quasi-free electronic states in the plane

parallel to the surface. These quasi-free electronic states exhibit parabolic energy dispersions as a function of the electron \mathbf{k} -vector parallel to the surface (see Figure 2). At the n -alkane/Ag(111) interface, image state electrons become spatially localized in the direction parallel to the surface.⁵ Ge *et al.*⁶ have used angle-resolved femtosecond TPPE to show that electrons initially in the extended image states self-trap into a spatially localized small polaron within a few hundred femtoseconds. The energy dependence of the self-trapping rate has been modeled with a theory analogous to electron transfer theory. In addition to the study of the spatial localization process of electrons at interfaces, a series of elegant experiments utilizing time-resolved TPPE have measured hot electron decay,^{7–9} excited quantum well state lifetimes,¹⁰ charge carrier dynamics in semiconductors,^{11,12} and coherent oscillations.¹³ These experimental findings have furthered our understanding of the importance of substrate and adsorbate band structure on electron relaxation processes.

Femtosecond TPPE has been widely utilized in the study of hot electron dynamics at metal surfaces.^{7–9} Absorption of photons at metal surfaces results in a transient nonthermal distribution of electrons or hot electrons. Ogawa *et al.* have recently studied hot electron dynamics at the Cu(100), Cu(110), and Cu(111) surfaces.⁷ Their results on the energy dependence of the lifetimes deviate from the Fermi liquid theory for free-electron metals. (Fermi liquid theory has a functional form of $\tau \propto (E - E_F)^{-2}$ for the relaxation time where E_F is the Fermi level and E is the energy of the hot electron with respect to the Fermi level.) Their electron–electron scattering calculations, assuming a Thomas–Fermi screening length, gave lifetimes that were a factor of 6 shorter than those measured. These discrepancies were attributed in part to the d-band electrons at about 2 eV below E_F , which can participate in both scattering and screening of hot electrons. Similar results were independently observed by Cao *et al.* on Cu(100).⁹ In addition, the recent development of interferometric time-resolved two-photon photoemission by Ogawa *et al.* provides the opportunity to measure decoherence times that occur in tens of femtoseconds.¹⁴ Coherence between the excitation electric field and the optically induced electron-hole polarization may have considerable effect in modeling surface state and hot electron lifetimes that are <100 fs. Coherence effects in the optical excitation of metals were reviewed recently by Petek and Ogawa.¹⁵ As mentioned by the authors of the review, coherence effects in the optical excitation of metals in the femtosecond time scale is still a young field of study with many unsettled questions and a number of controversies.

Femtosecond laser pulses exhibit bandwidths on the order of tens of millielectronvolts, which are sufficient to excite a coherent superposition of several high quantum number image states ($n \geq 4$). The coherent superposition of these states results in wavepackets that oscillate between the image potential barrier and the metal surface barrier. Höfer *et al.*¹³ have shown that the electron wavepackets travel more than 200 Å away from the surface and oscillate back and forth in the well with a period of 800 fs at the Cu(100) surface. The photoemission intensity increases as the wavepackets move closer to the surface since the metal substrate provides the necessary momentum for photon absorption.

The primary focus of the present work consists of the study of the electron relaxation processes at metal surfaces in the presence of thin layers of insulating or wide energy gap materials. Using femtosecond TPPE, the lifetimes of image states and Xe conduction band quantum well (QW) states at the Xe/Ag(111) interface were measured.¹⁰ It will be shown

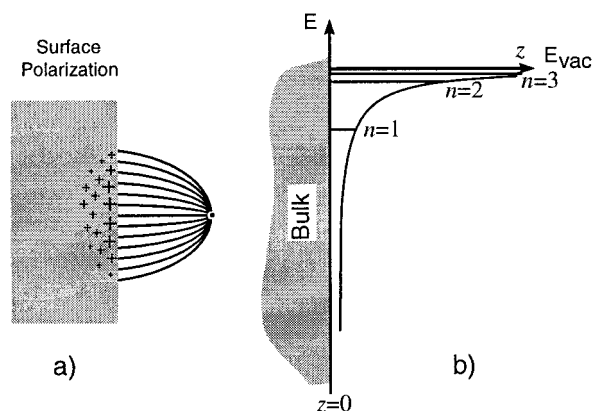


Figure 1. (a) An electron near a surface polarizes the material. This induced polarization binds the electron by forming a potential well that consists of the image potential. (b) Solving the analogous 1-D hydrogen atom problem gives rise to Rydberg-like or image states that converge toward the vacuum energy level E_{vac} .

below that the perpendicular spatial extent of the electronic wavefunction at the interface mainly determines the interband relaxation rate of electrons, that is, relaxation from the interfacial states to the metal bulk bands. Factors that influence the spatial extent of the interfacial electronic states include the nature of the interfacial potential barrier and the electronic properties of the two materials comprising the interface. The ability to grow thin insulating films on metals allows us to determine the change in the electronic properties at the metal–dielectric interface and the modification of the bare metal surface states upon adsorption of dielectric materials in a layer-by-layer fashion. Electron dynamics in the direction parallel to the Xe/Ag(111) interface, however, requires additional understanding of electron scattering with defects and phonons at the interface. Factors that affect the electron scattering rate in the direction parallel to the Xe/Ag(111) interface are discussed.

1.1. Surface Band Structure. The termination of a crystal results in states that are localized at the surface. Historical background and basic surface state theories have been extensively covered in a text by Davison and Stęślicka.¹⁶ Image states are a class of surface states that arise from the abrupt change in polarizability at an interface. An electron near the surface induces an image potential by polarizing the substrate (Figure 1a). This elementary electrostatic problem can be solved by the method of images,¹⁷ in which the electron at a distance z from the surface interacts with a fictitious image charge located at $-z$. This simple charge configuration satisfies all boundary conditions for an electric field in the presence of a perfect conductor and provides a unique solution to Poisson's equation: a $-1/4z$ Coulomb potential. The Coulomb potential gives rise to a series of Rydberg-like bound states that converges toward the vacuum energy, as shown in Figure 1b.

The surface band structure is represented by a projection of the three-dimensional band in the direction perpendicular to the surface, which is referred to as the projected bulk band structure (PBBS). This description of the surface bands accounts for the electronic properties of different crystallographic faces. In three dimensions, the crystal band structure is characterized by the band index number and the three-dimensional \mathbf{k} vector. In two dimensions, however, the surface band is characterized by the wave vector parallel to the surface \mathbf{k}_{\parallel} . For ordered surfaces, \mathbf{k}_{\parallel} is a good quantum number and is conserved in the photoemission process. The PBBS for the L -gap of Ag(111)¹⁸ is shown in Figure 2. Projecting the three-dimensional Brillouin zone yields the surface Brillouin zone (SBZ). The zone center of the

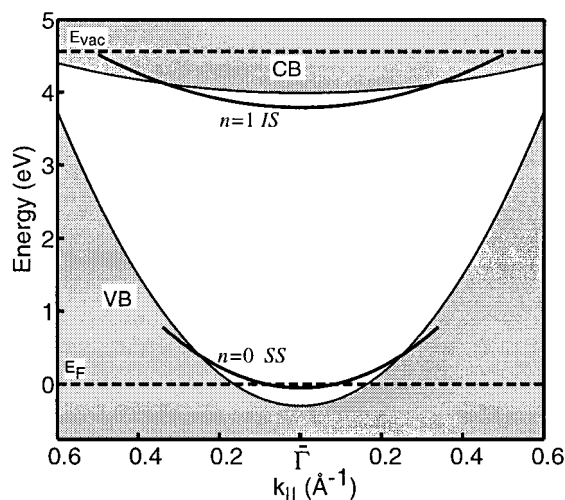


Figure 2. Projected bulk band structure of Ag(111). The zone center is labeled as $\bar{\Gamma}$ with increasing k_{\parallel} away from the zone center. CB and VB denote the conduction band and valence band, respectively. The shaded areas represent possible \mathbf{k} states that arise from projecting the 3-dimensional band structure into two dimensions. E_F is the Fermi level and E_{vac} represents the vacuum level. The boundary conditions at the surface allow the surface state (SS) and the $n = 1$ image state to reside in the L -gap.

SBZ is labeled as the symmetry point $\bar{\Gamma}$. Since the boundary conditions of surface states are different from the bulk electronic states, surface states may reside in the band gap of a material. In Figure 2 the surface state (SS) and the $n = 1$ image states are shown. Both states reside in the gap and disperse from the $\bar{\Gamma}$ point into the bulk electronic states. The wavefunction that describes these surface states are factored into two components, namely the perpendicular and the parallel components.¹⁹ The parallel part of the wavefunction is a free-electron-like plane or Bloch wave since in the parallel direction the periodicity is still retained. The perpendicular part of the wavefunction is an evanescent wave decaying both in the vacuum and in the bulk of the material. The characteristic wavefunction maximum at the surface renders surface electrons sensitive to changes in the electronic properties at the surface upon adsorption of thin films.

1.2. Multiple Reflection Theory (MRT). The hydrogenic model is the simplest model for image states. Its solution is obtained by solving Schrödinger's equation for an analogous one-dimensional hydrogen atom with the wavefunction vanishing at the surface. Because this model assumes that the electron is bound by an infinite potential at the surface, the hydrogenic model is not sensitive to crystallographic face. For more realistic metal surfaces the overlap of the image state wavefunction in the substrate is important in determining the binding energies and lifetimes. Since image state electrons interact with the many-body system of the substrate, which perturbs their motion, image state electrons are quasiparticles with "effective" or "renormalized" masses that are different from that of a bare electron. An elegant description of the effect of the metal surface projected band structure on image state effective mass has been detailed in an account by Giesen *et al.*²¹ Image state binding energies, lifetimes, and effective masses have been determined by both inverse photoemission and TPPE. Many of the values for transition metals have been tabulated in the review of Fauster and Steinmann.⁴ It was shown that the (111) crystallographic face of noble metals exhibit higher binding energies for image state electrons than the (100) face.

The multiple reflection theory (MRT)²² or phase-shift analysis does take into account the effect of the substrate band structure.

The image states are represented as plane waves that propagate between the reflecting barriers at the metal crystal band gap and the image potential in the vacuum. Bound states occur when the total accumulation of phase is $\phi_c + \phi_b = 2n\pi$, where ϕ_c and ϕ_b are the phase shifts accumulated at the crystal and image potential barrier, respectively. In the WKB approximation, the energy dependence of the phase at the image potential barrier is given by $\phi_b(E) = (2Z/\sqrt{-2E} - 1)\pi$, where E is the energy measured from the vacuum level and $Z = 1/4$ for a conductor. For energy levels near the tail of the image potential or near the vacuum level, ϕ_b increases with energy rapidly, yielding a Rydberg-like series. For image states that appear in a band gap of a metal which is s - p inverted, *i.e.* the conduction band is s -like while the valence band is p -like, the phase ϕ_c is approximately π when the energy level is close to the conduction band and 0 when it is near the valence band. The MRT formalism is a way to solve the matching conditions between the substrate wavefunction and the solution in the Coulomb potential in the vacuum. The matching conditions will determine the maximum of the wavefunction in the image potential. When ϕ_c is equal to π , the maximum of the wavefunction is closer to the surface and resides in the steep part of the Coulomb potential well. Thus, the image electron will be more bound. For the (111) crystallographic face of noble metals, the vacuum level resides in the conduction band. Since image states converge toward the vacuum level, the phase accumulated at the metal substrate for the image states will be $\phi_c \approx \pi$, resulting in image states that are more bound for the (111) crystallographic face of noble metals, as shown for the case of $n = 1$ for silver in Figure 3. The crystal phase shift of $\phi_c = 0.9\pi$ and $\phi_c = 0.5\pi$ were calculated for Ag(111) and Ag(100), respectively, by representing the band structure of silver with the two-band nearly free-electron model.

1.3. Two Band Nearly Free Electron Model. The two-band nearly free-electron (NFE) model effectively factors in the essential physics that determines the electron wavefunction overlap with the bulk. In the 1-D two-band NFE model, the crystal potential of the ion core is expanded in a Fourier series in multiples of the reciprocal lattice vector by the following:

$$V(z) = \sum_m V_{mg} e^{imgz} \quad (1)$$

where g is the amplitude of the reciprocal lattice vector. The $m = 0$ term represents the energy at zone center of the valence band and is conveniently set to 0. For crystals with inversion symmetry, V_g is equal to V_{-g} . Keeping only the first two terms, the electron energies E with respect to the zero energy (taken to be the valence band energy at zone center) for the two-band NFE model are given by solving the secular equation

$$\begin{vmatrix} (\hbar^2/2m^*)k^2 - E & V_g \\ V_g & (\hbar^2/2m^*)(k-g)^2 - E \end{vmatrix} = 0 \quad (2)$$

where V_g is the gap half-width and m^* is the effective mass along the surface normal. Within the gap, the solutions corresponding to real E require the wave vector k to be a complex quantity with the real and imaginary parts equal to p and q , respectively. The imaginary part q causes the wave to decay exponentially into the metal. Assuming the Bloch form of the electronic wavefunction,²³ the wavefunction perpendicular to the surface in the crystal is given by

$$\psi_c = e^{qz} \cos(pz + \delta) \quad (3)$$

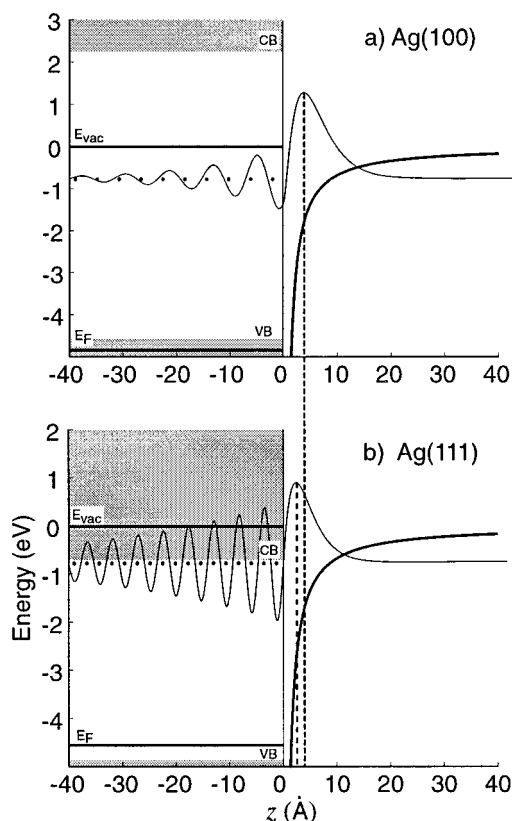


Figure 3. Band gap at $k_{\parallel} = 0$ for (a) Ag(100) and (b) Ag(111). The $n = 1$ image state wavefunction at the Ag(111) surface has $\phi_c \approx 0.9\pi$, which results in the maximum of the image state electronic wavefunction being closer to the metal and closer to the steep part of the image potential as compared to electronic wavefunction of Ag(100) with $\phi_c \approx 0.5\pi$. The calculated $n = 1$ state binding energies for Ag(111) and Ag(100) are -0.76 and -0.54 eV, respectively. The image potential close to the surface ($z = 0$) is set to a constant to avoid a singularity. CB and VB are the conduction and valence bands, respectively. E_F and E_{vac} are the Fermi level and vacuum level. The calculated electron densities in the metal are 0.54 and 0.10 for the Ag(111) and Ag(100) surfaces, respectively.

This solution for the crystal substrate corresponds to an evanescent wave decaying into the metal substrate in the metal band gap. Matching the boundary conditions of an incident plane wave with energy E to eq 3 results in ϕ_c , as given by the following equation:

$$\phi_c = 2 \arctan \left(\frac{p}{\kappa} \tan[pz + \delta] - \frac{q}{\kappa} \right) \quad (4)$$

where κ is the wave vector of the plane wave.

1.4. Dielectric Effects at Xe/Metal Interfaces. Outside the metal, the simple Coulomb potential of an excess electron at a metal surface can be altered significantly by adsorption of materials that change the dielectric susceptibility of the interface. The potential near the surface of metals in the presence of adsorbed dielectric materials, such as He, Ne, and H_2 films, was first modeled by Cole²⁴ by using the dielectric continuum approximation. The dielectric continuum approximation treats the overlayer as a dielectric continuum in which the electronic structure of the individual atoms or molecules are ignored. The potential felt by an electron depends on the location of the electron, namely inside or outside the dielectric overlayer near the overlayer/vacuum interface. In the limit of an infinite overlayer thickness, an electron in the vacuum outside the layer will only polarize the dielectric material, which gives rise to a

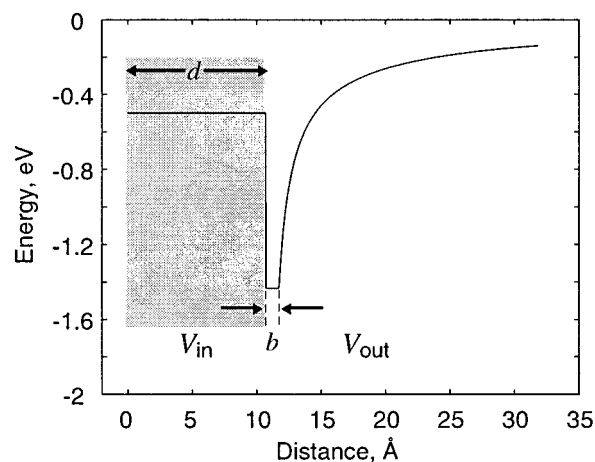


Figure 4. Potential used in calculating the quantum well states shown here is for three layers of Xe. The potential in the metal ($z < 0$) is given by the two-band NFE model. The potential in the layer is set to the Xe conduction band minimum or the affinity level of $V_0 = -0.55$ eV. The potential in the vacuum is the continuum electrostatics solution for the electron outside a dielectric layer on a metal substrate, as given by eq 6. A constant cutoff of length b is set near the surface of the dielectric to avoid a singularity. The thickness of the layer is denoted by d .

Coulomb potential equal to the first form of eq 6. Reducing the number of layers introduces additional terms that result from the proximity of the electron with the metal. The additional terms are represented as an infinite series. Inside the overlayer, the potential experienced by an electron is mainly attributed to the band structure of the overlayer. The potential inside the overlayer of Xe is taken as the Xe conduction band minimum of 0.55 eV below the vacuum energy level.^{10,20} The net effect of the Xe crystal potential on the motion of the electron is represented by the Xe conduction band effective mass of $m^* = 0.57m_e$.²⁰ The potential in the presence of Xe overlayers, as shown in Figure 4, is separated into two parts, namely inside and outside the Xe slab, as follows:

$$V_{in}(z) = V_0 \quad 0 < z < d \quad (5)$$

$$V_{out}(z, d) = \frac{-\beta e^2}{4(z-d)} + \frac{(1-\beta^2)e^2}{4\beta} \sum_{n=1}^{\infty} \frac{(-\beta)^n}{z-d+nd}, \quad d+b < z \quad (6)$$

where z is the distance from the metal, $V_0 = -0.55$ eV is the electron affinity of Xe, d is the layer thickness, b is a cutoff parameter to avoid a singularity at the dielectric/vacuum interface, ϵ is the dielectric constant of the Xe material, and $\beta = (\epsilon - 1)/(\epsilon + 1)$. The summation in eq 6 is the infinite series that describes the electrostatic potential experienced by the electron outside the dielectric layer.

2. Electronic Wavefunction and Electron Dynamics at the Xe/Ag(111) Interface

Thin overlayers of Xe on metals serve as model systems for understanding the electronic structure of both metal/insulator and metal/semiconductor interfaces due to the large band gap (on the order of 10 eV)²⁵ and high excess electron mobility (on the order of 10^3 cm²/V·s)²⁶ of the Xe crystal. The attractive electron affinity or conduction band minimum of $V_0 = -0.55$ meV of Xe allows electrons to reside in the Xe overlayer, which results in Xe conduction band QW states. In order to fully account for the binding energies and the lifetimes of image and

QW states at the Xe/Ag(111) interface, the band structure of both the metal substrate and the Xe overlayer must be taken into account. Since Xe physisorbs onto metal surfaces, the band structure of the substrate can be assumed to be relatively unperturbed by the adsorption of Xe. The Ag(111) substrate was treated as a two-band NFE, while the potential outside the metal substrate was treated as a dielectric continuum, as discussed in section 1.4. Other QW systems such as QW states of a metal layer on a metal substrate have been modeled as a two-band NFE overlayer on a two-band NFE substrate with an image potential in the vacuum.^{27,28}

2.1. Spatial Extent of Image and QW States at the Xe/Ag(111) Interface. By treating the metal with the two-band NFE model, the layer as a flat Xe conduction band minimum with $m^* = 0.57m_e$, and outside the layer as a modified image potential, the binding energies and the electron dynamics for states residing at the Xe/Ag(111) interface were successfully modeled for up to nine layers of Xe[10,20]. As mentioned in section 1.3, the solution for the metal substrate corresponds to an evanescent wave decaying into the metal substrate. The slope and value of eq 3 are propagated numerically using a fourth- and fifth-order Runge–Kutta integrator with adaptive step sizes through the flat overlayer potential and out into the vacuum. The trial solutions are evaluated for a range of energies to find solutions for which the wavefunction vanishes at about 120 Å outside the layer. To include the penetration of the image and QW state wavefunctions in the metal substrate is important in determining the binding energies and is the basis for modeling the lifetimes of these states.^{29–32}

2.2. Electron Dynamics at the Xe/Ag(111) Interface. It is reasonable to assume that the primary decay pathway for $k_{||} = 0$ electrons at the Xe/Ag(111) interface is via electron-hole pair excitation in the substrate. Under this assumption, the lifetimes scale with the overlap of the wavefunction with the metal substrate.³² This is an interband relaxation process in which electrons in the image state band decay into the bulk states of the metal. The overlap of the wavefunction P is determined by integrating the normalized interface state wavefunction, Ψ , in the metal substrate,

$$P = \int_{-\infty}^0 \Psi^* \Psi \, dz \quad (7)$$

where the limit of integration is from the bulk of the metal at $z = -\infty$ to the surface of the metal at $z = 0$. The lifetime broadening Γ of the interfacial state can be related to the line width of the bulk state with the same energy $\Gamma_b(E)$ by setting $\Gamma = P\Gamma_b(E)$. The line width Γ is related to the lifetime τ by $\Gamma\tau = 660 \text{ meV}\cdot\text{fs}$. The QW and image state lifetimes can be reproduced by theoretical calculations of the lifetimes based on independent photoemission values of $\Gamma_b(E) = 0.13(E - E_F)$.³³ The experimental results for the $n = 1, 2$, and 3 states for one to six layers of Xe on Ag(111) have been successfully modeled using this approach of wavefunction penetration in the metal.¹⁰ Wolf *et al.*³⁴ have applied this method to account for the lifetimes of $n = 1$ and 2 for a monolayer of Xe on Cu(111).

There are two important factors that affect the wavefunction penetration in the metal and therefore affect the interfacial state lifetime. The first factor corresponds to the relative position of the interfacial state with respect to the metal band structure. The penetration increases as the energy approaches the band edges and decreases as the energy is moved closer to the middle of the gap. This is demonstrated by the wavefunction calculations for Ag(111) and Ag(100) in Figure 3, which shows a significant decrease of the electron density in the metal for the

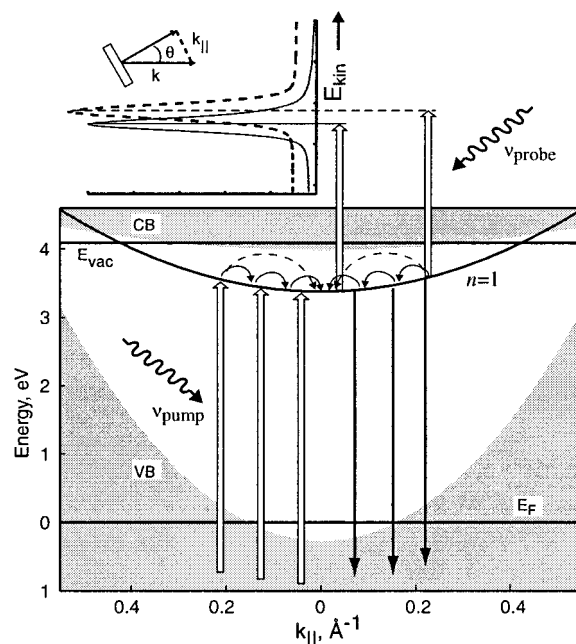


Figure 5. The L -gap PBBS of Ag(111) upon adsorption of a monolayer of Xe. The workfunction decreases to 4.06 eV and moves the $n = 1$ state further into the band gap. The left and the right side of the PBBS are used to illustrate the pumping and the probing process, respectively. The pump pulse (ν_{pump}) excites a distribution of $k_{||}$ states. Intraband relaxation processes occur after electron excitation into the image states, as shown by the curved solid and dashed arrows in the $n = 1$ image band. Interband relaxation can occur at every point in the $n = 1$ band, as shown by the downward solid-line arrows. Photoemission with the probe pulse (ν_{probe}) at various sample angles (θ) from the electron detector axis allows the mapping of the image state band and provides the opportunity to study electron momentum relaxation. k and $k_{||}$ are the total wave vector and parallel wave vector of the photoemitted electron, respectively.

Ag(100) $n = 1$ state. Using parameters from Echenique and Pendry,²² the electron densities in the metal for Ag(111) and Ag(100) are calculated to be 0.54 and 0.10, respectively. Lifetimes for the $n = 1$ and 2 image states have been measured for the Ag(111) and Ag(100) surfaces by Schoenlein *et al.*³⁵ Lifetimes of $n = 1$ and 2 were determined to be <20 fs for the Ag(111) surface. The Ag(100) $n = 1$ and 2 lifetimes, however, were determined to be 25 ± 10 and 180 ± 20 fs, respectively. It is important to note that intrinsic surface states and the location of the valence band with respect to the Fermi level play significant roles in determining image state lifetimes. For Ag(111), the presence of the surface state introduces an extra decay channel for the image state electrons. The surface state has a significant contribution to the $n = 1$ image state lifetime, as shown by Chulkov *et al.*³⁶ The extension of the Ag(111) band gap below the Fermi level, however, offsets the effect of the surface state by reducing the available phase space for electron decay.

The second factor that affects the wavefunction penetration is the adsorption of dielectric materials onto the metal surface. The addition of layers will either push the electronic wavefunction further away from the metal substrate or increase the width in which the electronic wavefunction can spread in the overlayer. The latter process occurs for electronic states that reside in the overlayer. Both effects increase the interfacial state lifetime.

While the wavefunction penetration successfully accounts for interband relaxation, an additional model is required to account for the strong parallel momentum dependence of the lifetime.

An electron in a particular $k_{||}$ state can undergo intraband relaxation to a lower momentum state. Mechanisms such as electron–electron, electron–defect, or electron–phonon scattering can contribute to the momentum relaxation rate (Figure 5). The study of dynamics as a function of parallel momentum allows us to explore the importance of reduced dimensionality, quantum confinement, and surface defects on the transport properties of carriers at interfaces.

3. Experimental Section

The dynamics results presented in this account were acquired by using an optical parametric amplifier (OPA) that was pumped by a 800 nm Ti:sapphire regenerative amplifier seeded by a Ti:sapphire oscillator. The OPA uses part of the 800 nm beam to generate white light continuum and 400 nm second harmonic. Parametric amplification of part of the white light gives wavelengths tunable from 500 to 730 nm with autocorrelation of about 100 fs after dispersion compensation.³⁷ It is advantageous to use two color TPPE to distinguish between the pumping and the probing process and to reduce background signal. Frequency doubling of visible light is especially suited for exciting electrons from the bulk occupied and surface-induced occupied states into image states residing at noble metal surfaces with work function on the order of 5 eV. The residual fundamental is used as the probe pulse. The instrument function was determined by fitting the dynamics of the occupied surface state at the $\bar{\Gamma}$ point of the Ag(111) PBBS (Figure 2) to a Gaussian function. Assuming that dephasing of the photon-induced electronic polarization is short compared to the pulse width, a cross correlation of the UV–visible photons can be derived from this state since excitation from this state is a coherent two-photon absorption through a virtual intermediate state. With the direct determination of t_0 (time delay at which the UV and the visible pulses are directly overlapped) and the Gaussian instrument function, it is possible to fit the measured kinetic traces to a convolution of the Gaussian instrument function with exponential decay functions to determine lifetimes that are considerably shorter (≈ 30 fs) than the instrument function. The instrument function for 305 nm pump and 610 nm probe is on the order of 100 fs.

3.1. Momentum Relaxation and Effective Mass Measurements. In order to obtain a well-ordered and clean sample, the Ag(111) surface was sputtered with Ar⁺ at 500 K and annealed at 725 K. The order and cleanliness were monitored by low-energy electron diffraction (LEED), Auger electron spectroscopy, and TPPE spectroscopy. For a well-ordered surface, the momentum component parallel to the surface is conserved during the photoemission process. The parallel dispersion $E(k_{||})$ of an energy band is determined by detecting electrons at various sample angles with respect to the electron energy analyzer (Figure 5). The momentum vector $k_{||}$ of the electron is given by

$$k_{||} = \sin \theta \frac{\sqrt{2m_e E_{\text{kin}}}}{\hbar} \quad (8)$$

where θ is the angle of the surface normal with respect to the detector, m_e is the free electron mass, and E_{kin} is the measured kinetic energy of the electron. The dispersion relation in the effective mass approximation is given by

$$E(k_{||}) = \frac{\hbar^2 k_{||}^2}{2m^*} + E_0 \quad (9)$$

where m^* is the effective mass of the electron parallel to the

surface and E_0 is the energy of the state at $k_{||} = 0$. The effective mass of the photoemitting state is readily determined by fitting a parabolic energy dispersion with the measured $E(k_{||})$. The effective mass is dependent on the coupling of the electron with the material at the interface. For example, the effective mass for the clean surface Ag(111) $n = 1$ image state is about $1.3m_e$, as determined by TPPE.^{21,38} After dosing four layers of Xe, the effective mass of the $n = 1$ state decreases to $0.6m_e$, which is closer to the bulk Xe value of $0.57m_e$.²⁰ This indicates that the state does have considerable overlap with the Xe layer. Initial excitation by a pump pulse creates a distribution of electrons over a range of $k_{||}$ states (Figure 5). Electrons in higher $k_{||}$ states can undergo both interband relaxation to the metal and intraband relaxation to lower $k_{||}$ states. The detector has a collection angle of $\pm 1.5^\circ$. For electron kinetic energy of 2 eV, the $k_{||}$ resolution is $\Delta k_{||} \approx 0.04 \text{ \AA}^{-1}$. The highest $k_{||}$ state that can be populated with a 305 nm pump and 610 nm probe is $k_{||} \approx 0.4 \text{ \AA}^{-1}$ for the $n = 1$ state. The energy of $n = 1$ at this $k_{||}$ value is close to the vacuum energy.

3.2. Physisorption of Xe on Ag(111). The process of growing Xe on Ag(111) requires the use of high-purity gas and a ultrahigh vacuum (UHV) chamber to minimize contamination of the layer. The sample was cooled by a liquid helium cryostat to temperatures as low as 45 K. The UHV chamber background pressure was less than 1×10^{-10} Torr. Layers can be grown by back-filling the chamber with Xe gas at pressures and sample temperatures specified by the phase diagram of Xe on Ag(111).³⁹ At a Xe pressure of about 2×10^{-6} Torr and at temperatures between 82 and 68 K, a monolayer of Xe formed, while at temperatures between 67 and 66 K, a bilayer formed. Xenon layers were grown by metered dosing of the cooled sample at 70 K for a monolayer and at 45 K for multilayer. After two layers, the Xe coverage is not uniform and peaks corresponding to more than one coverage are visible in a given spectrum, as shown in Figure 6. Whether the layer is grown by metered dosing by time (nonequilibrium conditions) or by back-filling (equilibrium conditions), Xe forms an incommensurate hexagonal layer on the Ag(111) surface, as determined by Xe/Ag-(111) X-ray structure results.⁴⁰

The adsorption of Xe changes the workfunction Φ at the metal surface. The workfunction shift $\Delta\Phi$ was accurately determined by analyzing the convergence of the image state series to the vacuum level using the quantum defect formula of $E_b = -0.85/(n + a)^2$, where n is the quantum number and a is the quantum defect parameter. The binding energies of the image states with respect to the vacuum level can be determined by solving the quantum defect parameter a for the image state series. We observed most of the workfunction change in our TPPE spectra for the first layer ($\Delta\Phi = -0.50$ eV) with a small shift for the second layer ($\Delta\Phi = -0.04$ eV) and no experimentally discernible shift for the third layer. The work function shift was also confirmed by fitting threshold ultraviolet photoemission data to a Fowler plot.⁴¹

4. Results and Theory for Interband Relaxation

The TPPE spectra of Xe/Ag(111) at various thicknesses of Xe are presented in Figure 6. Binding energies as a function of Xe coverage are plotted in Figure 7. Adsorption of a monolayer of Xe decreases the work function of Ag(111), which lowers the $n = 1$ state to about 0.5 eV below the Ag(111) conduction band minimum and places the $n = 1$ state further into the Ag-(111) band gap (Figure 8). The adsorption of a monolayer of Xe changes the binding energy of $n = 1$ from -0.77 to -0.68 eV. As shown in Figure 8, $n = 1$ is still 0.18 eV below the Xe

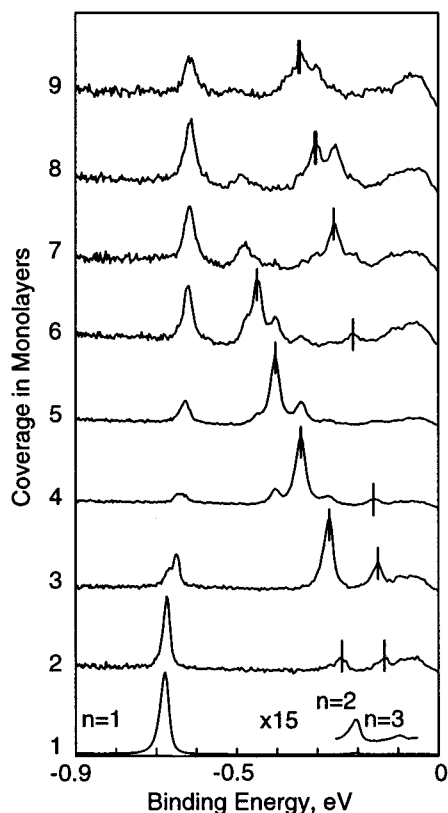


Figure 6. Static two-photon photoemission spectra of Xe/Ag(111) at a series of coverages (1–9 atomic layers, approximately). After two layers, the coverage is nonuniform, and peaks corresponding to more than one coverage are visible in a given spectrum. The dark line through the peaks indicates which peak is assigned to the coverage (in monolayers) indicated at the left of the figure. A nonlinear background was subtracted from the spectra in order to enhance the clarity of the features. This figure is reproduced with permission from ref 20, Figure 1. Copyright 1996 AIP.

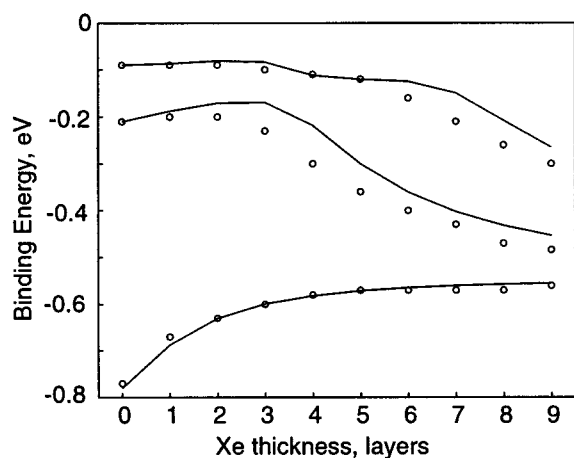


Figure 7. Comparison between experimental binding energies for the $n = 1, 2, 3$ states as a function of layer thickness (symbols) and the prediction of the quantum well model by using the potential shown in Figure 4. This figure is taken from ref 20, Figure 9. Copyright 1996 AIP.

conduction band edge. The $n = 2$ and 3 states, however, are energetically above the Xe conduction band minimum. The experimental results reveal that the binding energy of the $n = 1$ state decreases by 16% over the range of one to nine layers of Xe. The calculation of the $n = 1$ wavefunction for a range of Xe coverage shown in Figure 9 illustrates that the $n = 1$ electronic wavefunction is pushed further from the metal

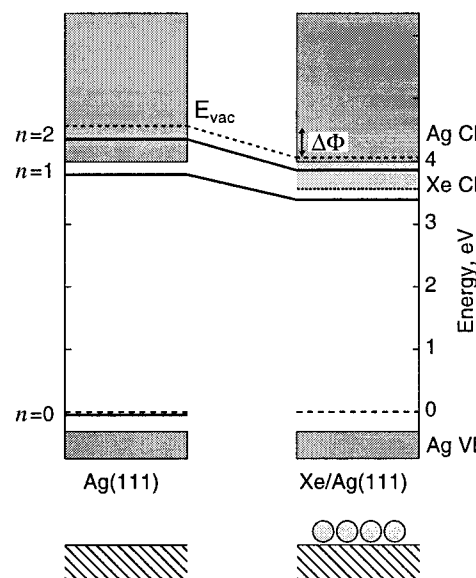


Figure 8. The adsorption of a monolayer of Xe decreases the work function of Ag(111) from 4.56 to 4.06 eV. This places the $n = 1$ state about 0.5 eV below the Ag(111) conduction band minimum; meanwhile, its energy is about 0.18 eV below the Xe conduction minimum. The $n \geq 2$ image states, however, are energetically above the Xe conduction band.

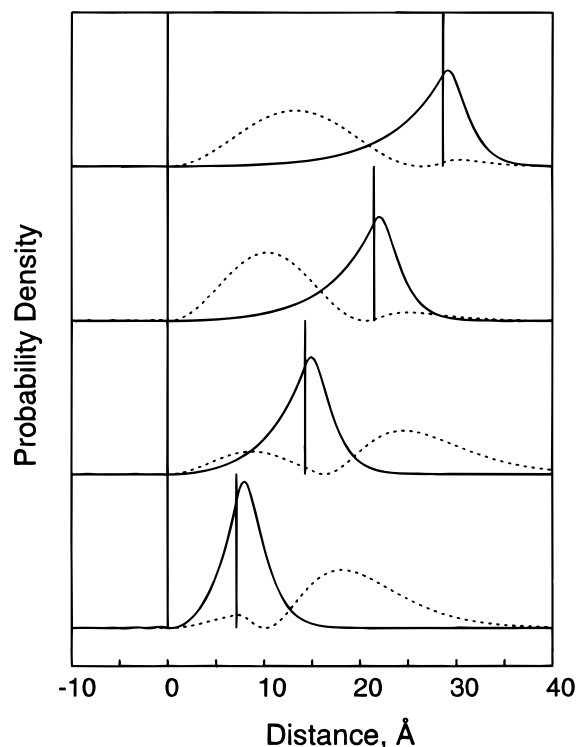


Figure 9. Resulting probability densities for the dielectric continuum model for the $n = 1$ (solid lines) and $n = 2$ (dashed lines) states for two, four, six, and eight layers of Xe on Ag(111). The bulk dielectric constant of $\epsilon = 3.0$ and electron affinity of $V_0 = -0.55$ eV were used. This figure illustrates the tendency of the $n = 1$ state to have significant wavefunction density at the dielectric/vacuum interface rather than in the dielectric slab. Meanwhile, the $n = 2$ state looks like a hydrogenic $n = 2$ image state at lower coverages but tends to move inside the layer and have a node near the dielectric/vacuum interface, which is indicative of a quantum well state of the Xe conduction band, for thicker layers. This figure is reproduced from ref 20, Figure 10. Copyright 1996 AIP.

substrate by the Xe potential. This affects the $n = 1$ image state lifetimes since the wavefunction overlap with the metal substrate

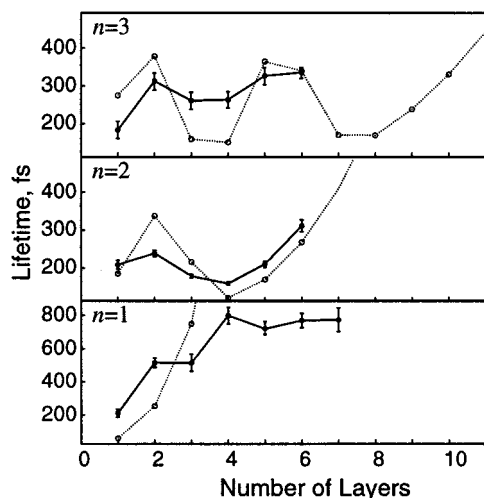


Figure 10. Lifetimes of the $n = 1, 2$, and 3 states for one to six layers of Xe extracted from the time-resolved data (filled circles). Lifetime predictions taken from the 1-D model (open circles) are in qualitative agreement with the oscillations in lifetime apparent in the data. The experimental error bars are calculated for a 95% confidence limit. The solid and dotted lines are only a guide to the eyes for experimental and calculated lifetimes, respectively. This figure is reproduced from ref 10, Figure 2b. Copyright 1997 APS.

decreases as the electron density is further away from the metal. In contrast, the $n = 2$ and 3 state binding energies monotonically increase, as expected for the formation of the Xe conduction band QW. The important difference between the $n = 1$ state and $n = 2$ and 3 states is that $n = 1$ is energetically within the Xe band gap, while the $n = 2$ and 3 states are degenerate with the Xe conduction band. Calculations show that the $n = 2$ and 3 states evolve into the Xe conduction QW states by moving into the Xe layer. Calculated wavefunctions for $n = 2$ are also shown in Figure 9.

The clean Ag(111) $n = 1$ image state lifetime was determined to be 30 ± 6 fs at 50 K. The lifetime was longer than the value measured by Schoenlein *et al.*³⁵ who determined the lifetime to be < 20 fs at room temperature. Upon adsorption of a monolayer of Xe, the lifetime of $n = 1$ increases to 240 fs (Figure 10). Overlapping features for multilayer and low signal level at high Xe coverage limited the time-resolved TPPE spectra to one to six layers of Xe. The best fit to the data requires a short exponential rise, which we assume to be attributed to k_{\parallel} relaxation to lower k_{\parallel} states within the image state band (Figure 5). A portion of the rise time, however, may be due to the coherence dephasing.^{15,34} The $n = 1$ lifetime increases monotonically with each additional layer of Xe. This results from the decrease in wavefunction overlap with the metal substrate since the $n = 1$ wavefunction is pushed toward the vacuum, as shown in Figure 9.

The lifetime of the $n = 2$ and 3 states exhibits lifetime oscillations as a function of layer thickness, which is caused by the quantum size effect (Figure 10). An understanding of these oscillations can be gained by considering the perpendicular expectation value for the hydrogenic image states. In the hydrogenic model, the expectation value of z for the wavefunction in the image potential is given by $\langle z \rangle = 6a_0n^2$, where a_0 is the Bohr radius. The expectation value of z for $n = 2$ is about 12.7 Å. By looking at the wavefunction of the $n = 2$ state in Figure 9, the crossover of the $n = 2$ image state to a QW state appears at a Xe layer thickness of four layers. Four layers of Xe correspond to a thickness of about 14 Å. This result can be interpreted as follows. For the monolayer, the states are only

slightly perturbed from those of the clean surface because of the small spatial overlap of the layer potential with the hydrogenic (zero-order) wavefunction. When the layer is thick enough for significant overlap with the zero-order hydrogenic wavefunction where $d \approx \langle z \rangle$, the image state moves into the layer and the energy is brought down by the attractive Xe layer potential. Since $n = 3$ has $\langle z \rangle \approx 29$ Å, its binding energy is significantly brought down in the range of seven to nine layers. It is also interesting to note that the $n = 2$ lifetime has a minimum at four layers of Xe. Since the $n = 2$ wavefunction can move into the Xe layer at four layers, this allows the wavefunction to be closer to the metal and to increase its overlap with the metal substrate. This higher wavefunction penetration in the metal substrate reduces the lifetime of the $n = 2$ image state, and we see a dip in its lifetime at four monolayers of Xe (Figure 10). After the dip in the lifetime of the $n = 2$ state, the lifetime starts to increase again. The increase in the $n = 2$ lifetime at higher coverage indicates the spreading of the $n = 2$ wavefunction in the Xe overlayer.

5. Intraband Relaxation

The lifetime of the $n = 1$ state shows a strong parallel momentum dependence (Figure 11). The penetration of the electronic wavefunction discussed in section 2.2 does not explain the strong parallel momentum dependence of the image state electron lifetime. For the PBBS of Ag(111), as shown in Figure 2, the wavefunction overlap of $n = 1$ with the metal substrate will increase as a function of k_{\parallel} since the state disperses toward the conduction band. The change of the wavefunction penetration for image states off the zone center can only account for a faster decay of a few percent for the small k_{\parallel} values in this study. The inability of the wavefunction overlap in the metal to account for the pronounced parallel momentum dependence of the interfacial state lifetime necessitates the consideration of intraband relaxation process. The dynamics of electrons with non-zero parallel momentum are affected by imperfections at the interface. Either thermal or structural disorder at the surface will cause a decrease in the electron mean free path (MFP) in the direction parallel to the surface. The experiments that measure both momentum relaxation and intraband relaxation of interfacial electrons allow us to explore the effect of reduced dimensionality and quantum confinement on carrier transport properties.

Intraband relaxation can be caused by electron–electron, electron–phonon, and electron–defect scattering. The scattering of electrons with acoustic phonons and impurities are often termed as quasi-elastic scattering since the energy change after collision is on the order of a few millielectronvolts. Thus, the main result of quasi-elastic scattering is momentum relaxation.⁴² Scattering of electrons will cause an increase in photoemission line widths. Line widths as a function of k_{\parallel} of the Cu(111) occupied surface state were measured by Kevan and co-workers.⁴³ They found a broadening of the photoemission line width as a function of k_{\parallel} , which they attributed to a non-lifetime effect, an electron–impurity elastic scattering process. Since both lifetime effect and weakened k_{\parallel} conservation can cause line width broadening, line width measurements alone may not give reliable information on population decay. Time-resolved TPPE, however, gives us a direct measure of the electron population as a function of time. The strong parallel dependence of the image state lifetime is attributed to momentum relaxation. Possible momentum relaxation processes are discussed below.

5.1. Momentum-Resolved Lifetimes. The lifetime of the $n = 1$ state for a monolayer and bilayer of Xe was measured at

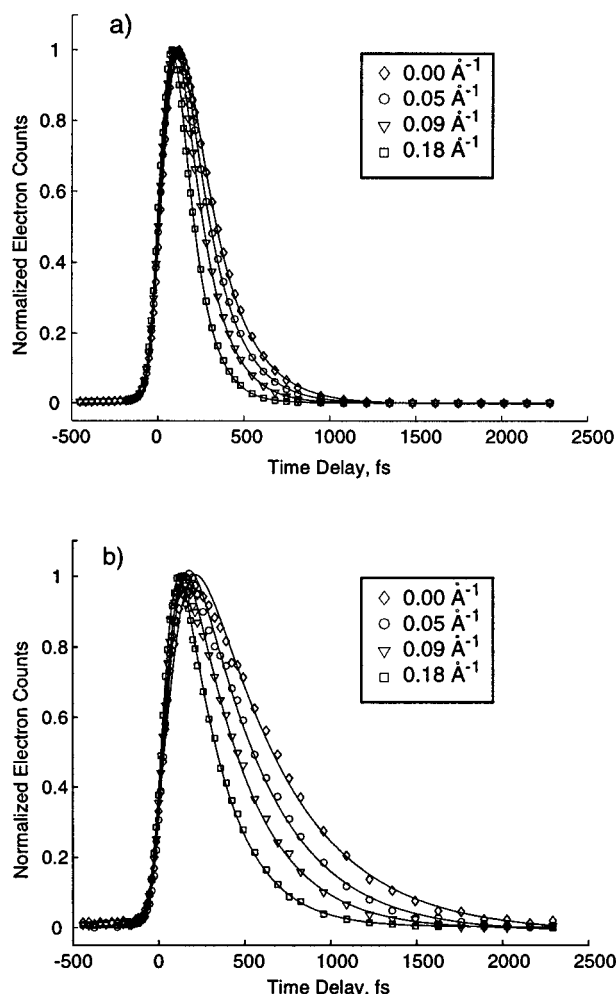


Figure 11. Momentum-resolved femtosecond TPPE dynamics traces for the $n = 1$ state for (a) a monolayer and (b) a bilayer. In both cases, the lifetime decreases by about a factor of 2 in going from $k_{\parallel} = 0$ to $k_{\parallel} = 0.18 \text{ \AA}^{-1}$. Symbols denote the data points, and the solid lines through the data points are fits to determine the lifetimes. The fits are convolutions of the Gaussian instrument function with exponential decay and rise functions.

various sample angles to study electron momentum relaxation as a function of layer thickness. Traces of the lifetimes at different k_{\parallel} states are shown in Figure 11. For both the monolayer and bilayer, the lifetime decreases monotonically as the electron parallel momentum increases. The lifetime of the monolayer $n = 1$ decreases from 211 ± 10 to 117 ± 5 fs for $k_{\parallel} = 0$ and $k_{\parallel} = 0.18 \text{ \AA}^{-1}$, respectively. For the bilayer, the $n = 1$ state lifetime decreases from 557 ± 50 to 254 ± 20 fs for states with $k_{\parallel} = 0$ and $k_{\parallel} = 0.18 \text{ \AA}^{-1}$, respectively. In both cases, the lifetime decreases by about a factor of 2 in going from $k_{\parallel} = 0$ to $k_{\parallel} = 0.18 \text{ \AA}^{-1}$. The rise time for the monolayer $n = 1$ state decreases from 60 to 37 fs for states with $k_{\parallel} = 0$ and $k_{\parallel} = 0.18 \text{ \AA}^{-1}$, respectively. For the bilayer, the rise time decreases from 86 to 42 fs. The decrease in the rise time is consistent with a process that feeds population from higher k_{\parallel} states into lower k_{\parallel} states. It was mentioned previously that the energy of the pump pulse at 305 nm will populate a distribution of k_{\parallel} states of $n = 1$ all the way to the vacuum energy level, approximately $k_{\parallel} = 0.4 \text{ \AA}^{-1}$. The electron dynamics results for $n = 1$ as a function of parallel momentum are tabulated in Table 1.

The decay pathways for states with finite parallel momentum can mainly be separated into two parts as follows. One can assume that the total lifetime depends on the interband relaxation and the intraband relaxation process. To separate out the

TABLE 1: Rise and Decay Times of $n = 1$

$k_{\parallel} (\text{\AA}^{-1})$	monolayer $n = 1$		bilayer $n = 1$	
	rise (fs)	decay (fs)	rise (fs)	decay (fs)
0.00	60	211	86	557
0.05	54	186	70	440
0.09	47	156	58	352
0.18	37	117	42	254

TABLE 2: $n = 1$ Line Widths

$k_{\parallel} (\text{\AA}^{-1})$	monolayer $n = 1$		bilayer $n = 1$	
	Γ_{T} (meV)	Γ_{\parallel} (meV)	Γ_{T} (meV)	Γ_{\parallel} (meV)
0.00	3.13	0.00	1.18	0.00
0.05	3.55	0.42	1.50	0.32
0.09	4.23	1.10	1.88	0.70
0.18	5.59	2.46	2.60	1.42

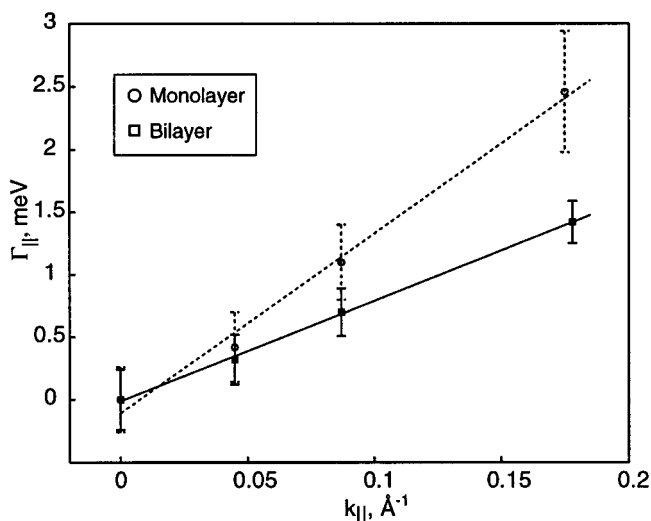


Figure 12. Line width Γ_{\parallel} as a function of k_{\parallel} of the $n = 1$ state for a monolayer and bilayer of Xe. The plot has a linear k_{\parallel} dependence. The monolayer slope is steeper than the bilayer, which shows that electrons are scattered more effectively for the monolayer Xe/Ag(111) interface than for the bilayer.

intraband contribution to the lifetime, we converted lifetimes to line widths. The relaxation rate or scattering rate of a state is proportional to the line width. The total lifetime is related to the line width broadening due to the interband and intraband relaxation processes by

$$\frac{660 \text{ meV} \cdot \text{fs}}{\tau} = \Gamma_{\perp} + \Gamma_{\parallel} = \Gamma_{\text{T}} \quad (10)$$

where τ is the total lifetime or decay time, Γ_{\perp} is the line width due to interband relaxation, Γ_{\parallel} is the line width contribution from intraband relaxation, and Γ_{T} is the total line width. Γ_{\parallel} is calculated as follows. Assuming Γ_{\perp} is independent of parallel momentum, Γ_{\perp} is equal to Γ_{T} at $k_{\parallel} = 0$. Using eq 10, Γ_{\parallel} is calculated by subtracting Γ_{\perp} from Γ_{T} for all angles. These values are shown in Table 2. Γ_{\parallel} as a function of k_{\parallel} is plotted in Figure 12.

5.2. Electron Scattering Processes. Echenique *et al.*³⁰ have discussed the possibility of electron–electron interactions, which cause momentum relaxation of image state electrons. Image state electrons can interact with the high density of electrons in the metal substrate. This interaction is a Coulomb interaction, which gives rise to an Auger process and a line width contribution that is proportional to k_{\parallel}^4 . The line width of the $n = 1$ state, however, linearly depends on k_{\parallel} instead of k_{\parallel}^4 , as shown in

TABLE 3: $n = 1$ MFP for Monolayer and Bilayer of Xe

$k_{ }$ (\AA^{-1})	monolayer $\lambda(\text{\AA})$	bilayer $\lambda(\text{\AA})$
0.09	630	1050
0.18	570	1040

Figure 12. For a monolayer and bilayer of Xe, the adlayer will weaken the effect of electron–electron interaction between image state electrons and the bulk electron density and weaken the effect of the $k_{||}^4$ dependence of the line width.

Momentum relaxation via electron–phonon scattering can also occur in the subpicosecond time scale. The efficiency of electron scattering with phonons in the bulk depends on the deformation potential, the softness of the phonon modes, and the temperature of the sample. Bulk Xe has a soft phonon mode, as indicated by its low Debye temperature of 65 K.⁴⁴ The deformation potential represents the electron–phonon coupling strength. Study of the temperature dependence of the momentum resolved $n = 1$ lifetime was attempted for a monolayer of Xe. Due to the minimum attainable temperature of the experimental setup and the temperature at which the monolayer of Xe will desorb rapidly, the study was done at both 50 and 66 K. The lifetime of $n = 1$ at a given parallel momentum, however, did not change in this temperature range.

The slope shown in Figure 12 is proportional to the change in the scattering rate as a function of the change in $k_{||}$. The slope for the monolayer and bilayer are 14 and 8 $\text{meV}\cdot\text{\AA}$, respectively, which shows a considerably higher scattering rate as a function of $k_{||}$ for the monolayer. Intraband scattering due to phonons in bulk materials in the high temperature limit can be approximated by the following equation:⁴²

$$\frac{1}{\tau_p} = \frac{\sqrt{2}a_c^2(m^*)^{3/2}k_B T E^{1/2}}{\pi\hbar^4\rho\nu_s^2} \quad (11)$$

where a_c is the volume deformation potential, T is the temperature, k_B is the Boltzmann constant, ρ is the crystal density, and ν_s is the velocity of sound. The slope calculated using the parameters⁴⁵ $\nu_s = 0.804 \times 10^5$ cm/s, $a_c = 1.4$ eV, $\rho = 3.73$ g/cm³, and $T = 50$ K gives a slope that is about 22 $\text{meV}\cdot\text{\AA}$. It is important to note that this calculation estimates the scattering rate of an electron residing in the bulk of solid Xe.

Electron–defect scattering plays an important role in the electron momentum relaxation process. Defects due to structural disorder of the Xe layer can be introduced by growing Xe at low temperatures such that the probability of obtaining an annealed Xe layer is reduced.⁴⁶ Structural disorder of the Xe layer may arise from vacancies in the Xe film.⁴⁵ Neutral impurity scattering in semiconductor for slow electrons have been modeled by Erginsoy⁴⁷ as scattering of electrons with hydrogen atoms. This model has been applied by Pleniewicz *et al.* to calculate the impurity scattering contribution to the electron MFP in bulk Xe.⁴⁵ The energy dependence of the MFP was implicitly accounted for by the energy dependence of the effective mass. The scattering rate calculated using this model, however, is independent of the electron energy for an image state electron that has a constant effective mass. The thickness dependence in the scattering rate as discussed above suggests that the monolayer of Xe exhibits stronger scattering sites than the bilayer. If this thickness dependence results from electron–impurity scattering, the neutral impurity model does not accurately represent the scattering potentials for this system. It is important to note that the bilayer presumably is more disordered than the monolayer. Calculations of the electron MFP

for higher $k_{||}$ states for both the monolayer and bilayer are shown in Table 3.

6. Closing Remarks

Momentum-resolved femtosecond TPPE provides a unique opportunity to study the effects of quantum confinement and reduced dimensionality on interfacial electron dynamics. The lifetime oscillation of $n = 2$ and 3 for $k_{||} = 0$ electrons were attributed to a quantum size effect that governs the interband relaxation process. From the measured momentum-resolved lifetime, transport properties such as electron MFP can be determined. This is the first attempt to separate out the contribution of interband and intraband relaxation processes by using momentum-resolved femtosecond TPPE. Intraband relaxation of $n = 1$ for a monolayer and bilayer should mainly be determined by electron–phonon and electron–defect scattering. The results show a considerable thickness dependence of the scattering rate and therefore an increase in the electron MFP from a monolayer to a bilayer. Defects such as vacancies in the Xe layer will give rise to scattering sites whose strength will depend on the layer thickness since the change in the interface potential is more abrupt from clean to monolayer than from monolayer to bilayer. It should be noted that the electron wavefunction overlap with the Xe bulk is higher for the bilayer than for the monolayer. The bilayer is also presumably more disordered than the monolayer. Given the higher rate of scattering for the monolayer, it is suggested that the monolayer exhibits stronger scattering sites than the bilayer.

The possibility of electron–phonon scattering cannot be ruled out, but the temperature study does not favor electron–phonon scattering to be the primary process of electron momentum relaxation for the monolayer $n = 1$. Trilayer Xe momentum resolved and partial monolayer coverage experiments will further our understanding of the scattering potentials. The packing of the layers for different layer thickness should have a considerable effect on the electron dynamics. In calculating the electron–phonon scattering rate as a function of electron kinetic energy using eq 11, the reduced dimensionality and the wavefunction overlap with the Xe layer were not taken into account. In both the monolayer and the bilayer, the electron MFP is expected to be longer than for electrons residing in the bulk of a Xe crystal. Theoretical models that take into account the two-dimensional nature of the system, surface defect potential, changes in the density of states around the Fermi level as a function of $k_{||}$, and the dependence of the scattering rates on wavefunction overlap with the layer would seem most likely to explain the complex nature of electron carrier scattering.

Acknowledgment. This work was supported by the Director, Office of Energy Research, Office of Basic Energy Sciences, Chemical Sciences Division of the U.S. Department of Energy, under Contract No. DE-AC03-76SF00098. The authors acknowledge NSF support for specialized equipment used in some experiments described herein.

References and Notes

- (1) Avouris, P.; Walkup, R. E. *Annu. Rev. Phys. Chem.* **1989**, *40*, 173.
- (2) Harris, C. B.; Ge, N.-H.; Lingle, R. L., Jr.; McNeill, J. D.; Wong, C. M. *Annu. Rev. Phys. Chem.* **1997**, *48*, 711.
- (3) Haight, R. *Surf. Sci. Rep.* **1995**, *21*, 275.
- (4) Fauster, Th.; Steinmann, W. In *Electromagnetic Waves: Recent Developments in Research; Photonic Probes of Surfaces*; Halevi, P., Ed.; Elsevier: Amsterdam, 1995; Vol. 2, p 347.
- (5) Lingle, R. L., Jr.; Padowitz, D. F.; Jordan, R. E.; McNeill, J. D.; Harris, C. B. *Phys. Rev. Lett.* **1994**, *72*, 2243.
- (6) Ge, N.-H.; Wong, C. M.; Lingle, R. L., Jr.; McNeill, J. D.; Gaffney, K. J.; Harris, C. B. *Science* **1998**, *279*, 202.

- (7) Ogawa, S.; Nagano, H.; Petek, H. *Phys. Rev. B* **1997**, *55*, 10 869.
- (8) Aeschlimann, M.; Bauer, M.; Pawlik, S. *Chem. Phys.* **1996**, *205*, 127.
- (9) Cao, J.; Gao, Y.; Miller, R. J. D.; Elsayed-Ali, H. E.; Mantell, D. A. *Phys. Rev. B* **1997**, *56*, 1099.
- (10) McNeill, J. D.; Lingle, R. L., Jr.; Ge, N.-H.; Wong, C. M.; Jordan, R. E.; Harris, C. B. *Phys. Rev. Lett.* **1997**, *79*, 4645.
- (11) Bokor, J.; Storz, R.; Freeman, R. R.; Bucksbaum, P. H. *Phys. Rev. Lett.* **1986**, *57*, 881.
- (12) Haight, R.; Baeumler, M. *Phys. Rev. B* **1992**, *46*, 1543.
- (13) Höfer, U.; Shumay, I. L.; Reuss, Ch.; Thomann, U.; Wallauer, W.; Fauster, Th. *Science* **1997**, *277*, 1480.
- (14) Ogawa, S.; Nagano, H.; Petek, H.; Heberle, A. P. *Phys. Rev. Lett.* **1997**, *78*, 1339.
- (15) Petek, H.; Ogawa, S. *Prog. Surf. Sci.* **1997**, *56*, 239.
- (16) Davison, S. G.; Stešlicka, M. *Basic Theory of Surface States*; Oxford University Press Inc.: New York, 1992.
- (17) Smythe, W. R. *Static and Dynamic Electricity*; McGraw-Hill: New York, 1984.
- (18) Plummer, E. W.; Eberhardt, W. *Adv. Chem. Phys.* **1982**, *49*, 533.
- (19) Ashcroft, N. W.; Mermin, N. D. *Solid State Physics*; Saunders: New York, 1976; p 367.
- (20) McNeill, J. D.; Lingle, R. L., Jr.; Jordan, R. E.; Padowitz, D. F.; Harris, C. B. *J. Chem. Phys.* **1996**, *105*, 3883.
- (21) Giesen, K.; Hage, F.; Himpsel, F. J.; Riess, H. J.; Steinmann, W.; Smith, N. V. *Phys. Rev. B* **1987**, *35*, 975.
- (22) Echenique, P. M.; Pendry, J. B. *Prog. Surf. Sci.* **1990**, *32*, 111.
- (23) Goodwin, E. T. *Proc. Camb. Phil. Soc.* **1939**, *35*, 205.
- (24) Cole, M. W. *Phys. Rev. B* **1971**, *3*, 4418.
- (25) Schwentner, N.; Himpsel, F.-J.; Saile, V.; Skibowski, M.; Steinmann, W.; Koch, E. E. *Phys. Rev. Lett.* **1975**, *34*, 528.
- (26) Asaf, U.; Steinberger, I. T. *Phys. Rev. B* **1974**, *10*, 4464.
- (27) Smith, N. V.; Brookes, N. B.; Chang, Y.; Johnson, P. D. *Phys. Rev. B* **1994**, *49*, 332.
- (28) Ortega, J. E.; Himpsel, F. J.; Mankey, G. J.; Willis, R. F. *Phys. Rev. B* **1993**, *47*, 1540.
- (29) Echenique, P. M. *J. Phys. C* **1985**, *18*, L1133.
- (30) Echenique, P. M.; Flores, F.; Sols, F. *Phys. Rev. Lett.* **1985**, *55*, 2348.
- (31) Bausells, J.; Echenique, P. M. *Phys. Rev. B* **1986**, *33*, 1471.
- (32) de Andres, P. L.; Echenique, P. M.; Flores, F. *Phys. Rev. B* **1989**, *39*, 10 356.
- (33) Goldman, A.; Altmann, W.; Dose, V. *Solid State Commun.* **1991**, *79*, 511.
- (34) Wolf, M.; Knoesel, E.; Hertel, T. *Phys. Rev. B* **1996**, *54*, R5295.
- (35) Schoenlein, R. W.; Fujimoto, J. G.; Eesley, G. L.; Capehart, T. W. *Phys. Rev. B* **1991**, *43*, 4688.
- (36) Chulkov, E. V.; Sarria, I.; Silkin, V. M.; Pitarke, J. M.; Echenique, P. M. *Phys. Rev. Lett.* **1998**, *80*, 4947.
- (37) Lingle, R. L., Jr.; Ge, N.-H.; Jordan, R. E.; McNeill, J. D.; Harris, C. B. *Chem. Phys.* **1996**, *205*, 191; *Chem. Phys.* **1996**, *208*, 297.
- (38) Merry, W. R.; Jordan, R. E.; Padowitz, D. F.; Harris, C. B. *Surf. Sci.* **1993**, *295*, 393.
- (39) Unguris, J.; Bruch, L. W.; Moog, E. R.; Webb, M. B. *Surf. Sci.* **1979**, *87*, 415.
- (40) Dai, P.; Angot, T.; Ehrlich, S. N.; Wang, S. K.; Taub, H. *Phys. Rev. Lett.* **1994**, *72*, 685.
- (41) Fowler, R. H. *Phys. Rev. B* **1931**, *38*, 45.
- (42) Yu, P. Y.; Cardona, M. *Fundamentals of Semiconductors: Physics and Material Properties*; Springer-Verlag: Berlin, 1995.
- (43) Tersoff, J.; Kevan, S. D. *Phys. Rev. B* **1983**, *28*, 4267.
- (44) Kittel, C. *Introduction to Solid State Physics*, 6th ed. Wiley: New York, 1986; p 110.
- (45) Plenkiewicz, B.; Plenkiewicz, P.; Jay-Gerin, J.-P. *Phys. Rev. B* **1986**, *33*, 5744.
- (46) Bader, G.; Perluzzo, G.; Caron, L. G.; Sanche, L. *Phys. Rev. B* **1982**, *26*, 6019.
- (47) Erginsoy, C. *Phys. Rev. B* **1950**, *79*, 1013.